GEOFIZIKA VOL. 42 2025

DOI: https://dx.doi.org/10.15233/gfz.2025.42.10
Original scientific paper

Seismic activity and gravity field interpretation for subsurface fault detection on Mount Pandan, Indonesia

Eko Minarto *and Krystallyn Gracella Angeline*

Department of Physics, Sepuluh Nopember Institute of Technology, Surabaya, Indonesia

Received 20 January 2025, in final form 30 September 2025

Indonesia experiences intense volcanic and tectonic activity due to its strategic location between 6° N–11° S latitude and 95° E–141° E longitude, where several major tectonic plates converge. Physiographically, Mount Pandan is located in the modern Sunda Arc region within the Anticlinorium or Kendeng Zone. Previous research recorded a minor earthquake in 2016, indicating ongoing tectonic activity in the Kendeng Zone, connected to sub-magmatic activity observed in several hot springs in Banyukuning, Jari, and Selogajah. Using gravity data, we identify the relationship between tectonic and magmatic activity through 3D inversion modelling of subsurface structures. This analysis correlates with fault fracture density (FFD) for surfaces with faults or fractures. Identifying the focal mechanism is essential for constructing the fault model of the earthquake source. The movement of Earth's crust along the Kendeng Fault influences underlying magmatic processes. Evidence of this interaction includes low-density zones and sub-magmatic features, such as the presence of hot springs. Earthquakes around the mountain with magnitudes below 4.0 SR suggest a relationship between the movement of strike-slip faults and oblique reverse faults with magma ascent. 3D inversion modelling reveals four layers:

⇒ At a depth of 0–0.46 km, with an estimated density range of 1.69–2.69 g/cm^3, we interpret the layer as caprock, composed of pyroxene and host rock types.

⇒ The layer at 0.46–1.14 km, with a density range of 1.31–2.23 g/cm^3, is interpreted as a reservoir containing sand and clay rock types.

⇒ Andesite and volcanic breccia rocks make up the layer at 1.14–1.59 km, with a density range of 2.4–2.8 g/cm^3. It is thought to be caprock and intrusion (active fault).

⇒ We interpret the layer at 1.59–2.43 km, with a density range of 1.43–3.45 g/cm^3, as a heat source with basalt rock types and magma content.

These findings provide new insights into the subsurface structure and fault dynamics of the Kendeng Zone, contributing to a better understanding of tectono-magmatic interactions in seismically active regions.

Keywords: Kendeng Fault, Mount Pandan, gravity data, reservoir, earthquake

1. Introduction

1.1. Scope and significance

The Mount Pandan area exemplifies the tight coupling between tectonic deformation and magmatism in a convergent-margin setting (Takashima and Yudiantoro, 2019). Using 3D gravity inversion and detailed mapping of fault architectures, we demonstrate how regional faulting and subduction stresses forge magma pathways, fueling both volcanic eruptions and intrusive bodies. In turn, these intrusions reshape fault behavior and local stress fields, giving rise to a complex volcanic system characterized by diverse rock types and structural features. Understanding this feedback loop is essential for evaluating volcanic and seismic hazards, optimizing geothermal and mineral exploration, and refining subduction-zone geodynamic models that guide both scientific inquiry and regional development.

Island-arc gravity studies are crucial for hazard assessment and geothermal exploration due to their ability to reveal subsurface geological structures with high precision (Frey et al., 2022). By mapping variations in gravitational fields, these studies identify fault lines, magma chambers, and other tectonic features that signal potential volcanic or seismic hazards, enabling proactive risk mitigation. Simultaneously, they pinpoint areas of high heat flow and fluid circulation critical for geothermal resource identification, optimizing exploration efforts. This dual role enhances our understanding of dynamic earth processes, making gravity studies an indispensable tool for both safeguarding communities and harnessing sustainable energy in island-arc regions.

Gravity-derived density inversions are inherently non-unique because different subsurface structures can yield the same anomaly. We reduce this ambiguity by calibrating our density models with borehole logs, outcrop mapping, and published well-test and petrographic data, anchoring density–lithology correlations in independent evidence.

1.2. Research motivation and objectives

The Kendeng Zone, a tectonically active region in Indonesia, remains poorly understood in terms of its subsurface structure, posing a significant knowledge gap in geological research (Hutchings and Mooney, 2021). Despite its location within a complex subduction zone and its association with volcanic and seismic activity, limited geophysical data and comprehensive studies hinder a clear understanding of its fault systems, sedimentary basins, and potential magma reservoirs. This lack of detailed subsurface mapping restricts accurate hazard assessments and the evaluation of geothermal resource potential, underscoring the urgent need for advanced geophysical investigations to illuminate the Kendeng Zone's geological framework.

Our research investigates the subsurface structure beneath Mount Pandan through two primary objectives. First, we employ 3D gravity inversion to map density anomalies, providing a detailed representation of subsurface mass variations. Second, we correlate these density anomalies with fault fracture density to identify their spatial and structural relationships, revealing zones of enhanced fracturing or deformation. This integrated approach elucidates the tectono-magmatic coupling beneath Mount Pandan, offering insights into how tectonic processes and magmatic activity interact to shape the region's geological framework.

1.3. Geological and tectonic setting

Mount Pandan is an 897-meter-high volcano between three East Java cities: Nganjuk, Madiun, and Bojonegoro. Mount Pandan is in the current Sunda Arc's Anticlinorium, or Kendeng Zone (Alawiyah et al., 2022) (Fig. 1). Figure 1 illustrates the physiographic zonation of East Java, which reflects the island's complex tectonic and sedimentary history. The region is divided into several distinct zones trending predominantly east–west, each with unique geomorphological and geological characteristics. This physiographic framework is essential for understanding the tectono-magmatic interactions in East Java. The zonation helps delineate fault systems, sedimentary environments, and geothermal features relevant to gravity modelling, fault analysis, and magmatic studies. Multiple hot springs and heated soil near Mount Pandan, particularly in Banyukuning, Jari, and Selogajah, suggest sub-magmatic activity. The Bouguer anomaly from Central to East Java indicates a shift in the pattern of gravity anomalies near Mount Pandan, indicating magmatic activity beneath the surface (Oktoberiman et al., 2015).

Mount Pandan is a Pliocene volcano composed of andesite intrusions and volcanic breccia. Based on regional physiographic classification, Mount Pandan is located in the Kendeng Zone (Alawiyah et al., 2022; Harsolumakso et al., 2019). The Kendeng Zone north of the Java volcanic arc forms an east–west–oriented anticlinorium of deformed marine sediments directly north of the Ngawi Subzone. It is divided into western, central, and eastern segments, with Mt Pandan situated in the central sector. There, Pliocene Kalibeng marls and interbedded volcanic sandstones grade upward into shallow-marine Klitik limestones and marls, Sonde claystone–sandstone turbidites, and Lower Pleistocene Pucangan volcaniclastic sandstones, all capped by Upper Pleistocene andesitic lavas and breccias of the modern volcanic complex. Geological structures in the Pandan area trend mainly NE–SW and NW–SE, with a few W–E faults cross-cutting the succession (Thoha et al., 2014).

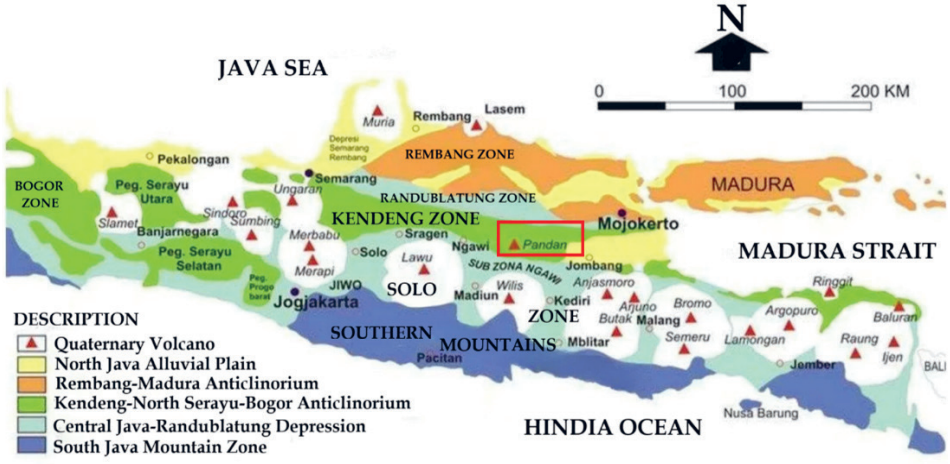

Figure 1. Physiographic zone of East Java.

In the Mount Pandan area, we developed a lithostratigraphic column by integrating systematic outcrop mapping with petrophysical logs from five boreholes. The sequence comprises Neogene marls, sandstones, and limestones overlying the Tertiary Kendeng basement, is overlain by Pleistocene andesitic lava flows interbedded with welded and non-welded tuffs, and is capped by Holocene–Pleistocene alluvial–colluvial clay, silt, sand, and gravel (Thoha et al., 2014; Agna and Jati, 2021). This integrated framework underpins our gravity-derived density correlations for delineating caprock and reservoir units.

In February 2016, small earthquakes struck near Mount Pandan, with magnitudes less than 4.0 SR at depths of roughly 10 km. Tectonic activity in the Kendeng Zone may play a role in driving magmatic processes beneath Mount Pandan. Therefore, characterizing the subsurface structure is essential to better understand this tectono-magmatic relationship (Harsolumakso et al., 2019).

1.4. Gravity method

The gravity method can be used to study and create 3D models of subsurface structures to find the connection between tectonic and magmatic activity in this area. We correlated this analysis with Fault Fracture Density (FFD) to identify anomalies that indicate the presence of magmatism and surfaces with faults or fractures (Ramadhani et al., 2018). Determining the focal mechanism is also critical to establishing the fault model of the earthquake source, which explains the relationship between tectonic and magmatic activity.

The presence of magma in an area is often due to faults or fractures caused by tectonic activity or the forces of pressure and tension affecting the rocks (Scandone et al., 2007). The alignment analysis process uses Digital Elevation Model (DEM) data to produce a fault density map, which can identify areas with the highest alignment. Earthquakes result from a sudden release of energy in the Earth's crust, creating seismic waves (Jain, 2014). The focal mechanism describes the nature of earthquake energy propagation centered at the hypocenter or focus of an earthquake. We can analyze the focal mechanism of an earthquake by determining the direction of fault motion and the fault plane, which closely links it to faults (Stauder, 1962).

The gravity method is a branch of geophysical science that measures variations in the gravitational field caused by differences in rock mass density below the Earth's surface (d'Amour Uwiduhaye et al., 2018). This study utilizes data from the Global Gravity Model Plus (GGM Plus) satellite to measure gravity. Gravity data processing using gravity disturbances (g_d) data from GGM Plus includes several correction stages, such as instrument readings, tidal, drift, and latitude corrections. Additional corrections are also required, including free air, terrain, Bouguer, and complete Bouguer anomaly correction (Dilalos et al., 2018).

Free Air Correction adjusts gravity values based on the elevation of the measurement point relative to sea level (mean sea level), ignoring the mass between them.

$$\Delta g_{FAA} = g_d + 0.3086h \tag{1}$$

Terrain or topographic correction accounts for the influence of irregular masses around the measurement point. Field measurement points like valleys and hills often have uneven topography, necessitating terrain correction (Nowell, 1999).

$$\Delta g_{T(r,\theta)} = G_{p\theta}\left\{(r_0 - r_i) + \sqrt{r_i^2 + \Delta z^2} - \sqrt{r_0^2 + \Delta z^2}\right\}. \quad (2)$$

The Bouguer correction addresses the mass effect between the measurement point and mean sea level (or datum). It decreases gravity values measured above sea level and increases those measured below sea level (Nowell, 1999; Tang and Sun, 2021).

$$\Delta g_B = 2\pi G\rho h = 0.04193\rho h\ . \quad (3)$$

These corrections yield the Complete Bouguer Anomaly (CBA) (Tang and Sun, 2021).

$$g_{CBA} = \Delta g_{FAA} - \Delta g_B + \Delta g_T \quad (4)$$

The CBA includes a combination of regional, residual (local), and noise anomalies (Minarto and Azhari, 2021). The spectrum analysis technique estimates the depth of an anomaly source in the frequency domain. Deep sources with low frequencies and long wavelengths cause regional anomalies, while residual anomalies are shallower than regional anomalies and noise. In contrast, residual anomalies are due to shallow sources with high frequencies and short wavelengths. A band-pass filter, which allows signals of specific frequencies to pass while blocking others, can isolate residual anomalies (Guo et al., 2013).

Geological structure interpretation can utilize residual anomalies. However, we can conduct further analysis, such as the first horizontal derivative (FHD) and second vertical derivative (*SVD*) analyses. *FHD* helps determine the continuity of a subsurface anomaly based on the horizontal first derivative (Minarto and Azhari, 2021; Setyawan, 2022).

$$FHD = \sqrt{\left(\frac{\partial g}{\partial x}\right)^2 + \left(\frac{\partial g}{\partial y}\right)^2}\ . \quad (5)$$

The SVD clarifies residual anomalies, making structures such as faults, fractures, anomalous objects, or discontinuities more visible. We derive the *SVD* equation from the Laplace equation (Susilawati et al., 2023).

$$\frac{\partial^2 g}{\partial z^2} = -\left(\frac{\partial^2 g}{\partial x^2} + \frac{\partial^2 g}{\partial y^2}\right). \quad (6)$$

The modelling process involves deriving a subsurface model from the Complete Bouguer Anomaly. This resulting model describes objects' density distribution and geometry at varying depths. In forward modelling, we calculate the data we would theoretically observe at the Earth's surface if we knew specific subsurface model parameters. Conversely, inverse modelling works the opposite: it derives the model parameters directly from the observational data. We often refer to this process as data fitting because it entails identifying the model parameters that yield a response that aligns with the observational data. We utilize inversion modelling to obtain helpful information about the distribution of subsurface modelling (Wang, 2023).

2. Methodology

2.1. Research methods

This study focuses on the Mount Pandan region of East Java, Indonesia, encompassing the districts of Madiun, Bojonegoro, and Nganjuk. The investigation area is defined in UTM Zone 49S coordinates, with eastings ranging from 569387.81 to 605871.61 and northings from 9163453.88 to 9199340.13 (Fig. 2).

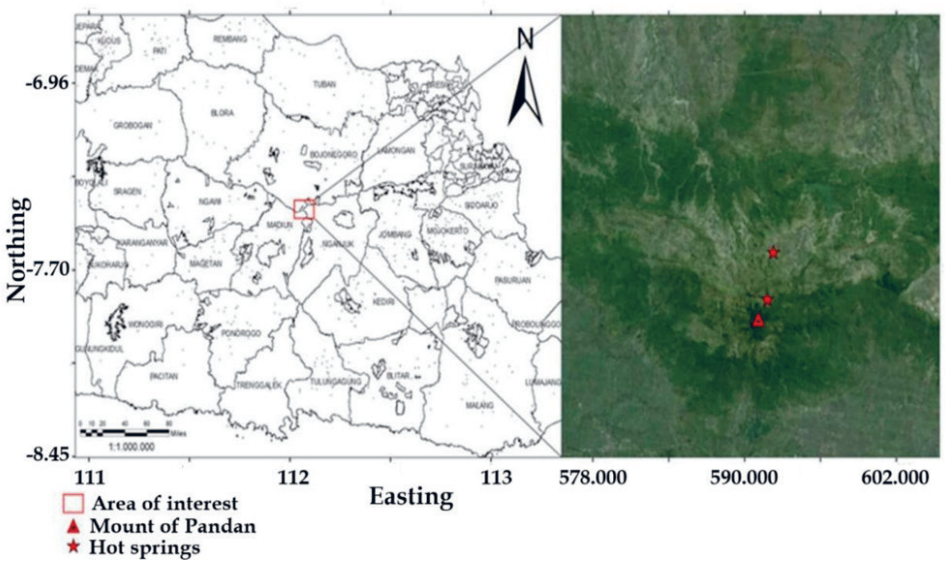

Figure 2. Research area of Mount Pandan.

We employed the gravity method to investigate subsurface structures, supported by multiple datasets:

- Digital Elevation Model (DEM) data for constructing free-air gravity maps
- Seismicity and focal mechanism data from Global CMT and BMKG for fault modeling
- Gravity data from Curtin University's GGM Plus database for anomaly analysis and 3D inversion modeling

Focal mechanism data from Global CMT were used to model fault orientations and types based on earthquake source parameters (Nakano et al., 2015).

2.2. Research workflow

The study commenced with a comprehensive literature review that synthesized recent advances in gravity methods and their geophysical applications, focal mechanism theory alongside seismicity distributions in East Java, and the geological and tectonic

frameworks characterizing the Mount Pandan region. To support our analysis, we compiled secondary datasets encompassing gravity disturbance measurements from Curtin University's GGM Plus repository (file S10E110), high-resolution elevation grids from DEMNAS and the ERTM2160 model, and seismicity and focal mechanism records from BMKG and the Global CMT initiative.

Using MATLAB, we processed the GGM Plus gravity grid (≈200 m resolution) with a custom script designed to import and parse raw data, delineate study-area boundaries by geographic coordinates, extract the target subset, and reformat the results into matrix structures suitable for further analysis. These gravity values were then integrated with the ERTM2160 elevation dataset to perform Bouguer and terrain corrections, laying the foundation for three-dimensional inversion modeling of Mount Pandan's subsurface architecture. This streamlined workflow ensured both high spatial fidelity and computational efficiency throughout the modeling process.

The data processing workflow comprised several integrated stages. Initially, Fault Fracture Density (FFD) maps were generated by converting DEMNAS elevation data into hillshade maps using ArcGIS, followed by automated lineament extraction via the LINE algorithm in Geomatica. Rosette diagrams were produced using RockWorks to visualize fracture orientations, and FFD maps were constructed in ArcGIS to quantify fracture density across the study area.

Gravity corrections were applied to geographic (longitude, latitude), topographic (elevation), and geophysical (geoid height, gravity disturbance) parameters using Oasis Montaj, resulting in Complete Bouguer Anomaly (CBA) maps. Anomaly separation was conducted using the MAGMAP module with a band-pass filter, employing a long-wavelength cutoff of 3000 m and a short-wavelength cutoff of 2200 m.

Spectral analysis of the radial average spectrum was performed to estimate regional depth, residual anomalies, and noise levels, utilizing linear regression techniques. Derivative analysis was applied to enhance structural interpretation, generating First Horizontal Derivative (FHD) and Second Vertical Derivative (SVD) maps using Oasis Montaj and Surfer.

Three-dimensional inversion modeling was conducted with Grablox and Bloxer, enabling volumetric visualization and cross-sectional interpretation of subsurface structures within a domain of 20 km (easting) × 20 km (northing) × 10 km (depth).

The final stage involved integrated interpretation, including fault modeling based on earthquake source parameters and FFD maps, and correlation with subsurface structures inferred from gravity data. The complete workflow is summarized in Fig. 3.

2.3. GGM plus gravity data

The gravity data for this study were obtained from the GGM Plus satellite mission, which continuously monitors variations in Earth's gravitational field along its orbital path. By tracking electromagnetic wave frequency shifts, the system detects minute changes in satellite velocity and position induced by gravitational anomalies, while differential accelerometry between adjacent spacecraft measures the local gravity-field gradient (Oberndorfer and Müller, 2002). Flying in a precisely controlled formation, the satellites employ laser interferometry and micro-range measurement systems to resolve inter-satellite distance changes on the order of micrometers, and they relay raw observa-

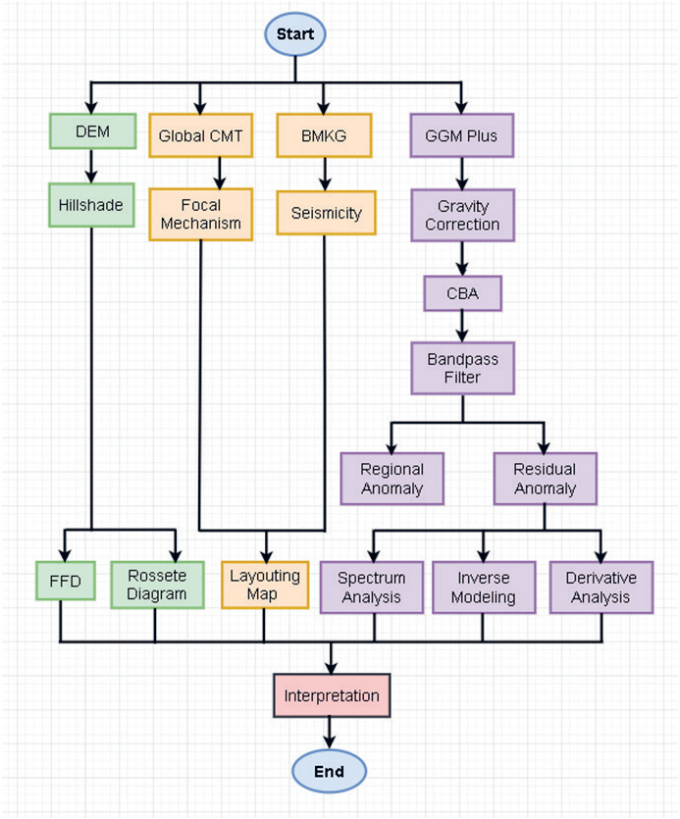

Figure 3. Research flowchart.

tions via radio telemetry to ground stations. Once received, these measurements are processed with advanced mathematical models and inversion algorithms to produce the high-resolution gravity anomaly maps that underpin our geophysical interpretations.

2.4. Rock density estimation

Through the parametric method, which synthesizes gravity measurements with geological and physiographic constraints, we quantified both the average Bouguer density and the total Bouguer anomaly across the Kendeng Zone. The analysis yielded an average Bouguer density of 1.71 g/cm^3, a value that faithfully reflects the composite lithology of this region—dominated by sandstone, clay, limestone, pyroxene andesite, and volcanic breccia. This density estimate not only aligns with established petrophysical data but also strengthens our subsurface structural models derived from the observed gravity anomalies. Corrected density logs were converted to porosity and calibrated against core-plug data to establish empirical porosity–permeability relationships. This unified calibration of density, porosity, and permeability yields a single petrophysical model for precise reservoir and caprock characterization.

2.5. Analysis Fault and Fracture Density

In this study, we performed a fault-and-fracture density (FFD) analysis around Mount Pandan. Lineaments were automatically extracted from high-resolution satellite imagery using a least-cost path algorithm in GIS. Orientation and density were quantified in 500 m × 500 m blocks. Hot-spring locations were compiled from field surveys and overlaid to assess spatial correlation with FFD patterns.

2.6. Spectral separation of gravity anomalies

The Complete Bouguer Anomaly (CBA) comprises signals from varying depths, including deep regional sources, intermediate structures, and shallow noise. To isolate these components, spectral filtering was applied using Fourier transformation, which converts spatial gravity data into the frequency domain.

In this domain, low-frequency signals correspond to deep-seated sources with broad spatial influence, while high-frequency signals reflect shallow, localized features. A band-pass filter was used to separate regional and residual anomalies by combining high-pass and low-pass filters. Cutoff wavelengths were set at 3000 m for long-wavelength (regional) components and 2200 m for short-wavelength (residual) components.

3. Results and discussion

3.1. Analysis Fault and Fracture Density (FFD)

Magmatic activity is strongly associated with faults and fractures (Ibrahim et al., 2021). When thermal fluids escape the surface, sub-magmatic activity manifests as hot springs. We conducted a fault and fracture density (FFD) analysis to understand the alignment density around Mount Pandan.

Figure 4a presents the distribution of extracted lineaments, revealing a predominant northwest–southeast orientation. The accompanying rosette diagram (Fig. 4b) confirms this NW–SE trend.

Lineament density varies spatially (Fig. 5):

- Highest densities (0.40–0.55 lineaments per km²) occur on the mid-slopes of Mount Pandan
- Moderate densities (0.25–0.40 lineaments per km²) appear around the volcano's flanks, coinciding with mapped hot-spring sites
- Lowest densities (< 0.25 lineaments per km²) cluster near the summit

These quantitative outputs define the structural framework without processing details. High FFD values indicate the presence of faults or fractures and associated magmatic activity. Areas with medium density often have hot springs. In regions with high alignment density, porosity is low due to fewer pores in the rock, preventing fluid accommodation and leading to alignment filled with igneous rock types (Heap and Violay, 2021).

The NW–SE alignment of fractures parallels the regional stress field imposed by the adjacent subduction zone, indicating tectonic control on fracture development. Elevated FFD on the slopes suggests enhanced permeability pathways that channel magmatic-derived fluids toward the surface, consistent with the spatial coincidence of hot springs in moder-ate-density zones.

Conversely, the summit's low FFD reflects dense volcanic deposits and fracture infill by later igneous intrusions, which reduces porosity and inhibits fluid migration. This

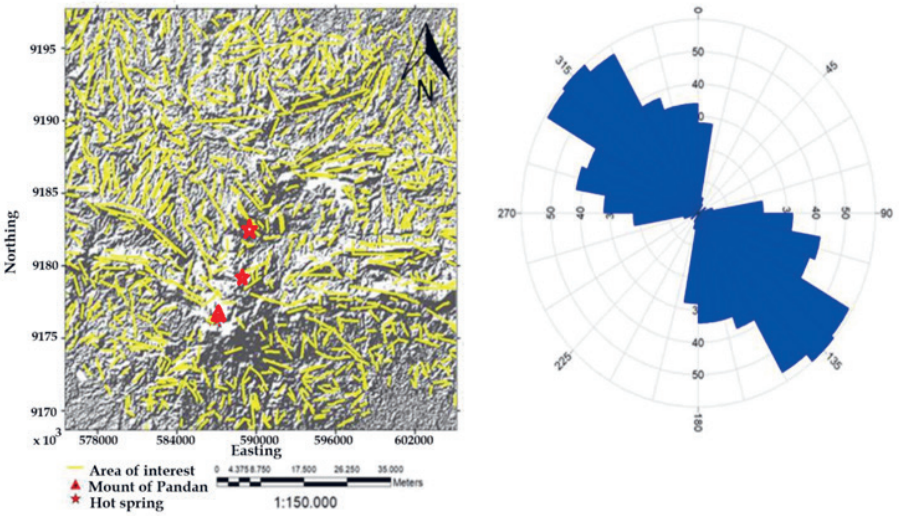

Figure 4. (*a*) Linearity map for the Mt Pandan area. Linear features (yellow lines) were extracted from a shaded-relief DEM and overlaid on a shaded-relief topographic base. Hot springs (red stars), Mt Pandan (red triangle) are shown for reference. The mapped lineaments reveal dominant structural trends oriented NW–SE, and (*b*) Rose diagram of lineament azimuths (10° bins), showing a dominant NW–SE trend.

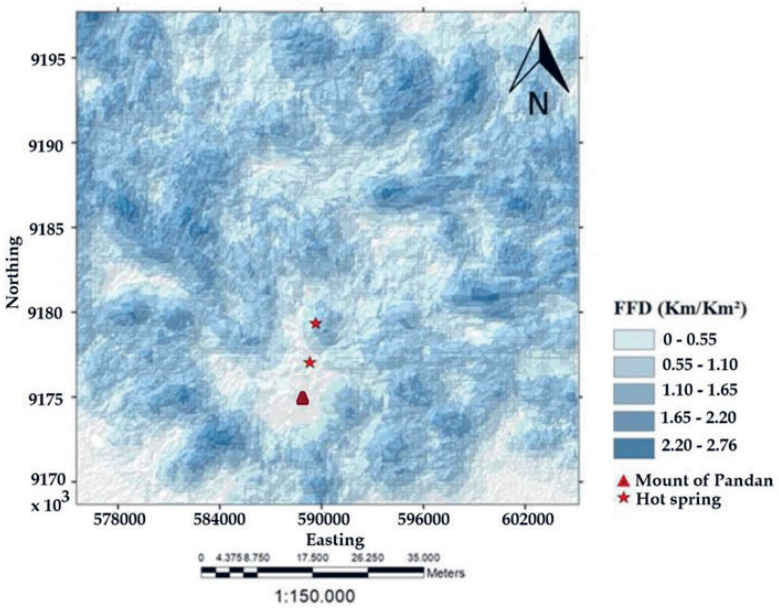

Figure 5. Lineament density map (Fracture Frequency Density, FFD) for the Mt. Pandan area. FFD is shown as a blue gradient heatmap with five classes: 0.00–0.55, 0.55–1.10, 1.10–1.65, 1.65–2.20, and 2.20–2.76 km/km². Mount Pandan is marked by a red triangle, and hot springs by red stars.

dichotomy between slope and summit fracture permeability highlights how structural architecture governs hydrothermal discharge at Mount Pandan and supports our overarching aim to link fracture networks with magmatic-hydrothermal processes.

3.2. Complete Bouguer Anomaly (CBA)

The Complete Bouguer Anomaly (CBA) was calculated by applying free-air, Bouguer, and terrain corrections to the gravity data. Coordinates were converted to UTM format (Zone 49S) for spatial analysis. Figure 6 presents the CBA distribution, with values ranging from 13.84 mGal to 39.79 mGal.

High anomaly values (shown in red to purple) are concentrated near Mount Pandan, particularly along the central segment of the Kendeng fault. The northern flank of Mount Pandan also exhibits elevated CBA values. These spatial patterns suggest localized zones of excess subsurface mass.

The concentration of high CBA values near Mount Pandan likely reflects the presence of dense magmatic bodies and intrusive rocks, which contribute to gravitational anomalies due to their elevated densities relative to surrounding lithologies.

The elevated CBA observed on the northern side of Mount Pandan may be influenced by the subduction-related tectonic architecture of the Randublatung depression zone and the Rembang hills. The Ngrau fault, which transects this region, marks a structural boundary between crustal blocks with contrasting geological characteristics. Depressions within the Randublatung zone are likely filled with dense sediments or subsurface structures such as faults and folds, resulting in localized mass concentrations and corresponding gravity highs.

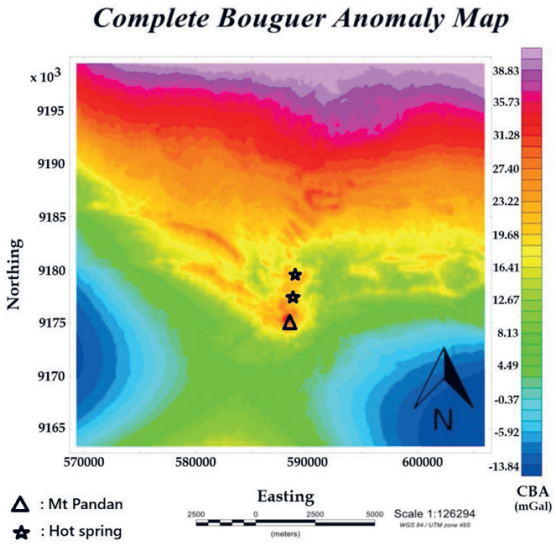

Figure 6. Complete Bouguer anomaly map of the study area (–13.84 to +39.79 mGal, blue–red), corrected for latitude, elevation, and terrain using a density of 1.71 g/cm^3. Gravity highs align with basement uplifts, while lows outline sedimentary basins.

3.3. Regional and residual anomalies

Figure 7a presents the regional anomaly map, with values ranging from –13.82 mGal to 29.79 mGal. These anomalies reflect deeper lithospheric variations and broad structural trends.

Figure 7b shows the residual anomaly map, isolating near-surface features with values between –1.01 mGal and 1.02 mGal. High residual gravity anomalies are concentrated around Mount Pandan and two nearby hot springs.

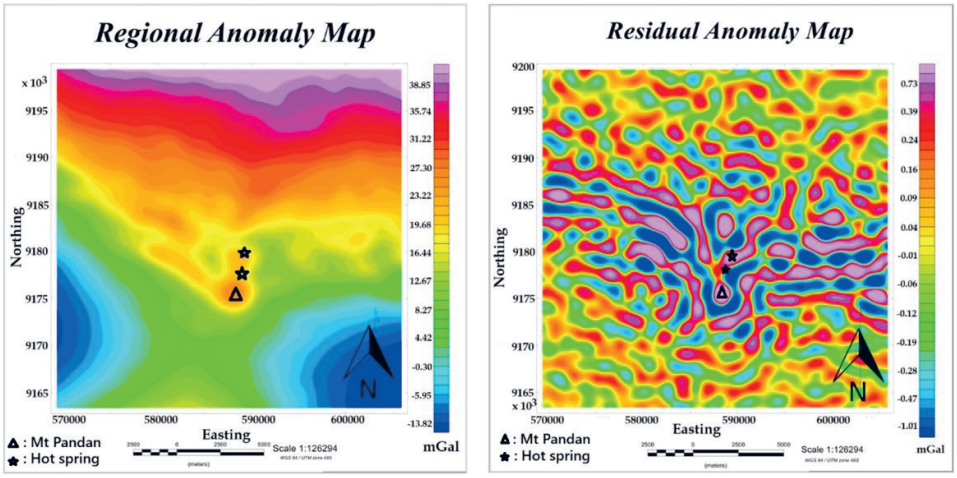

Figure 7. Maps of (*a*) complete regional anomalies map (–13.82 to +29.79 mGal; blue–red) with hot springs (stars) and major structural trends, and (*b*) residual anomalies map (–1.01 to +1.02 mGal; blue–red) for the study area showing gravity lows and highs with superimposed hot-spring locations (stars). Legend identifies gravity contours, volcanic centers, and hot springs.

The elevated residual anomalies near Mount Pandan and adjacent hot springs suggest the presence of dense igneous bodies, likely associated with magmatic intrusions. These features contrast sharply with surrounding areas dominated by low-density sedimentary units such as clay and sand.

The spatial distribution of residual anomalies supports the interpretation of fault-controlled magmatic activity and highlights subsurface heterogeneity across the study area.

3.4. Spectrum analysis

To estimate the depth of gravity anomaly sources, we applied Radially Averaged Power Spectrum (RAPS) analysis using a 2D Fourier Transform. This technique transforms spatial gravity data into the frequency domain and averages power values radially around the origin to produce a 1D spectrum.

The resulting graph (Fig. 8) plots the natural logarithm of spectral amplitude (ln A) against wave number (k), allowing separation of regional, residual, and noise components.

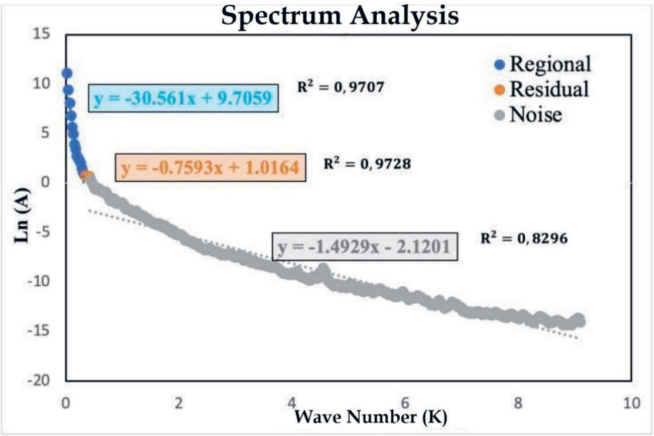

Figure 8. Spectrum analysis graph: plot of ln spectral amplitude (ln *A*) versus wave number (*k*), with fitted linear trends for regional (low-k), residual (mid-k) and noise (high-k) components. Axes are labeled ln *A* (dimensionless) and *k* (km^{-1}).

Linear regression was fitted to each segment of the spectrum to estimate depth penetration, following standard spectral analysis procedures (Loshin, 2011).

The RAPS analysis yielded the following depth estimates:

- Regional anomaly: 2.432 km
- Residual anomaly: 0.060 km
- Noise: 0.118 km

These values reflect the vertical extent of subsurface structures contributing to each gravity signal component. The horizontal axis of the spectrum represents spatial frequency (or wavelength), while the vertical axis indicates signal intensity across the frequency range.

The regional anomaly depth (~2.4 km) corresponds to deeper lithospheric structures beneath Mount Pandan, including magmatic intrusions, active fault zones, and the inferred back-arc basin setting.

The shallow residual anomaly (~60 m) likely reflects near-surface features such as volcanic deposits, fracture zones, and hydrothermal systems. The noise component (~118 m) represents minor surface heterogeneities and data artifacts.

These spectral results support the interpretation of a fault-controlled magmatic system with distinct structural layering, consistent with the gravity anomaly patterns and lineament analysis presented earlier.

3.5. Analysis of derivatives

To enhance the delineation of subsurface structures, we applied derivative analysis to the residual gravity anomalies using the First Horizontal Derivative (*FHD*) and Second Vertical Derivative (*SVD*). These filters are effective in clarifying gravity anomaly boundaries that are not readily visible in the original data.

FHD highlights lateral density contrasts by enhancing slope continuity, while SVD emphasizes vertical gradients, making it particularly useful for identifying compact or abrupt structural features (Sumintadireja et al., 2018). Fault zones, which typically exhibit density discontinuities due to stratigraphic offsets, can be detected through correlated patterns in *FHD* and *SVD* maps.

Figures 9a and 9b show the residual gravity anomalies after applying *FHD* and *SVD* filters:

- *FHD* values range from 0.00008 mGal to 0.00275 mGal, with higher values indicating steeper slopes and sharper lateral transitions
- *SVD* values range from –0.00000521 mGal to 0.00000552 mGal, visually enhancing anomaly boundaries and compact features

A prominent high-anomaly zone is observed near Mount Pandan, suggesting a localized density contrast.

To investigate potential fault structures, we performed a slicing analysis on both *FHD* and *SVD* maps (Fig. 10). The slice was oriented vertically along the suspected fault direction, guided by the derivative contour maps, geological maps, and other supporting datasets. Faults are inferred where the slicing graph shows:

- *SVD* values approaching zero or near-zero
- Coinciding *FHD* and *SVD* graph lines

These features indicate a layer shift or discontinuity consistent with fault-related density contrasts.

The derivative analysis reveals several anomalous boundaries, with the most prominent located near Mount Pandan. The correlated *FHD* and *SVD* patterns, along with the

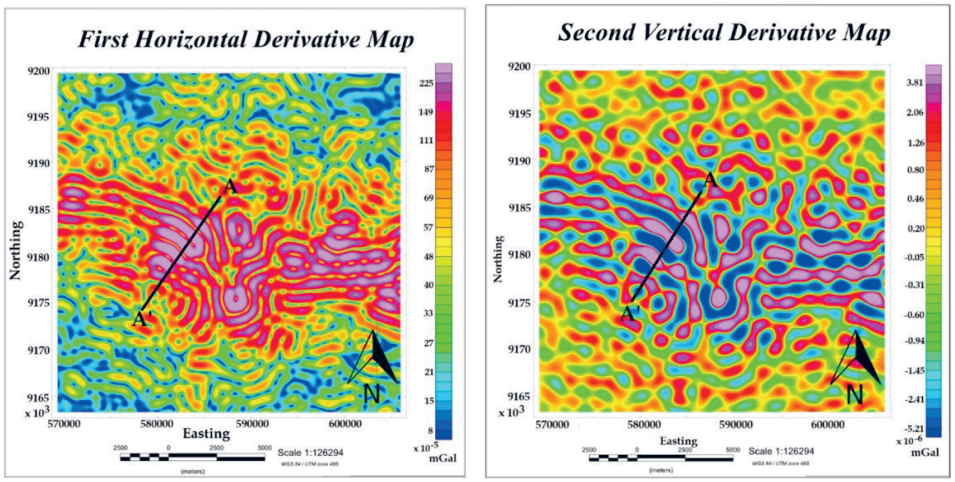

Figure 9. (*a*) First Horizontal Derivative (*FHD*) map showing lateral density contrasts and major fault zones, and (*b*) Second Vertical Derivative (*SVD*) map highlighting shallow subsurface features and localized anomalies.

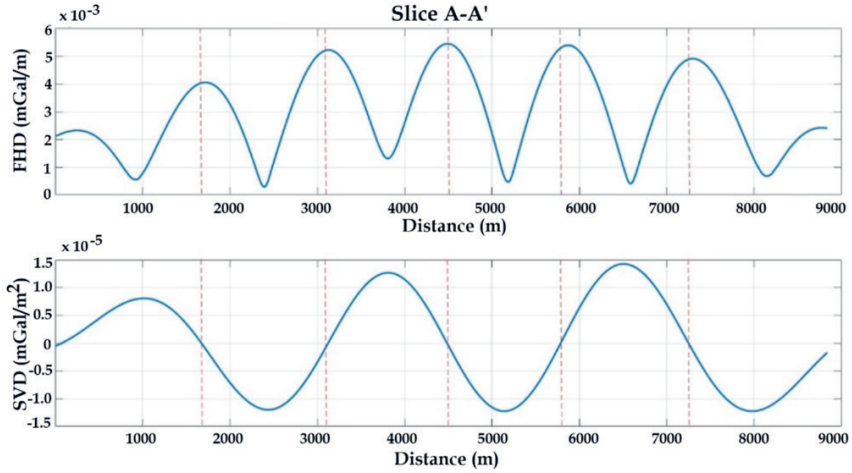

Figure 10. Slice extracted along Line A–A′ through (up) the First Horizontal Derivative (*FHD*), and (bottom) the Second Vertical Derivative (*SVD*) maps over Mount Pandan. The *FHD* profile enhances edge detection of normal fault planes via sharp gradient inflections, while the *SVD* profile delineates fault continuity and estimates dip angles, confirming the presence of extensional faults.

slicing results, support the presence of fault structures. These faults likely contribute to the observed gravity gradients and may play a role in controlling subsurface fluid migration or magmatic activity.

3.6. Analysis of seismicity and focal mechanism

Gravity anomaly modeling of the Mount Pandan region reveals a strong spatial correlation with regional seismic activity. Across East Java, BMKG and Global CMT catalogs record seismic events spanning moment magnitudes (M_W) 2.1–7.2 and hypocentral depths of 5–300 km. Within the Mt Pandan study area, earthquakes range from M_W 0.5 to M_W 3.9 at depths of 4–48 km, with most events ($M_W < 4$) clustering at shallow levels (5–35 km) along the Kendeng fault zone (Fig. 11).

Most recorded events are low-magnitude earthquakes or swarms, with magnitudes below 4 and no clearly defined mainshock. These events are concentrated at shallow depths (0–50 km), particularly along the Kendeng fault zone.

Beachball diagrams derived from focal mechanism solutions show that the dominant fault types in the region are strike-slip and oblique reverse faults, consistent with the structural orientation of the Kendeng fault.

Swarm earthquakes in the Mount Pandan area are likely driven by a combination of tectonic stress, fluid migration, and magmatic processes (Khan, 2013). The shallow depth and clustering of these events suggest active faulting within the upper crust, which may facilitate magma ascent.

The correlation between gravity anomalies, fault structures, and seismicity supports the interpretation that tectonic deformation along the Kendeng fault influences both seismic and magmatic activity.

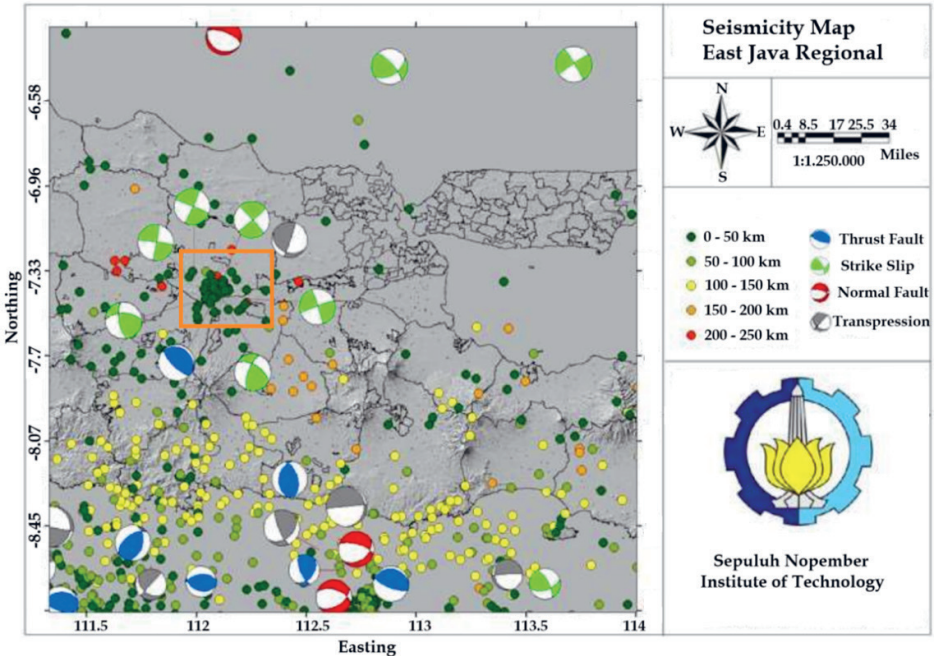

Figure 11. Seismicity distribution and focal mechanisms across East Java, Indonesia. Circles denote earthquake epicenters color-coded by hypocentral depth; beach-ball symbols represent focal mechanisms distinguishing thrust, normal, and strike-slip faulting. Region-wide, events span moment magnitudes (M_W) 2.1–7.2 and depths of 5–300 km. Within the Mt Pandan study area (inset), earthquakes range from M_W 0.5–3.9 at depths of 4–48 km, with most events (M_W<4) clustering at shallow levels (5–35 km) along the Kendeng fault zone.

The tectonic setting of Mount Pandan is governed by the subduction of the Indo--Australian plate beneath the Eurasian plate, forming a convergent margin and modern volcanic arc system. Fault activity within this zone can trigger magma migration toward the surface, contributing to volcanic manifestations such as Mount Pandan (Khan, 2013; Muttaqy et al., 2022).

3.7. Modeling inversion

To investigate subsurface structures associated with geothermal manifestations, we applied a four-stage gravity inversion workflow that integrates base-geometry optimization, iterative density refinement, block-height correction, and Occam regularization. Misfit analysis yielded error rates of 4.2 % at the base stage, 1.4 % for density optimization, 3.18 % during height adjustment, and 2.89 % following Occam smoothing. The Occam-regularized density contours demonstrate excellent agreement between observed and synthetic gravity fields, substantially reducing residual anomalies and enhancing model fidelity. Concurrently, height-optimized contours further minimize discrepancies in gravity anomaly values across data points, validating the robustness of our inversion approach and its effectiveness in resolving geothermal-related subsurface architectures.

Figure 12 presents the 3D inversion modeling results, revealing subsurface layers with densities ranging from 1.0 to 3.5 g/cm^3. The vertical extent of the model reaches 2.43 km, with lateral dimensions of 36.48 km along the east–west (X-axis) and 35.88 km along the north–south (Y-axis) directions. The primary block model is discretized along the X, Y, and Z axes, with spatial divisions denoted by dx, dy, and dz, respectively.

Figure 13 shows a cross-sectional view perpendicular to the Z-axis, illustrating the vertical layering and fault-related structures. To aid fault interpretation, we employed the first horizontal derivative map and the second vertical derivative map, which highlight discontinuities and structural boundaries. Additional details are provided in the appendices.

The 3D inversion modeling reveals a relatively consistent decrease in minor block height across the study area. Figures 14 and 15 illustrate cross-sectional profiles along the easting direction (573–604 km) and northing direction (9164–9188 km), respectively. These profiles show variations in both density and vertical extent of the minor blocks, suggesting active fault intrusion at depth. Additional structural details are provided in the appendices.

The observed variations in block height and density are indicative of localized deformation, likely associated with fault propagation and intrusion processes. These anomalies align with the broader tectonic framework inferred from gravity data and support the presence of active subsurface faulting.

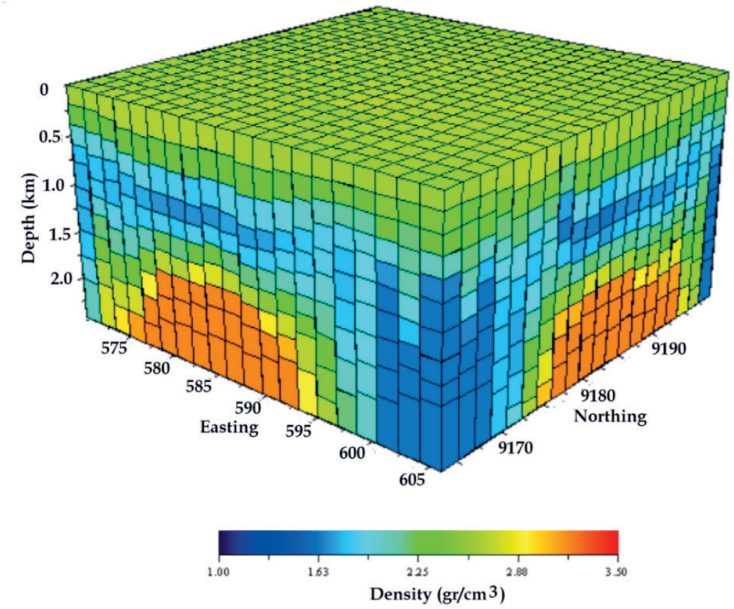

Figure 12. Three-dimensional inversion model of subsurface density contrast: A volume-rendered model of residual Bouguer gravity inversion results, color-coded for density contrast (1.00 to 3.50 g/cm^3; blue to red).

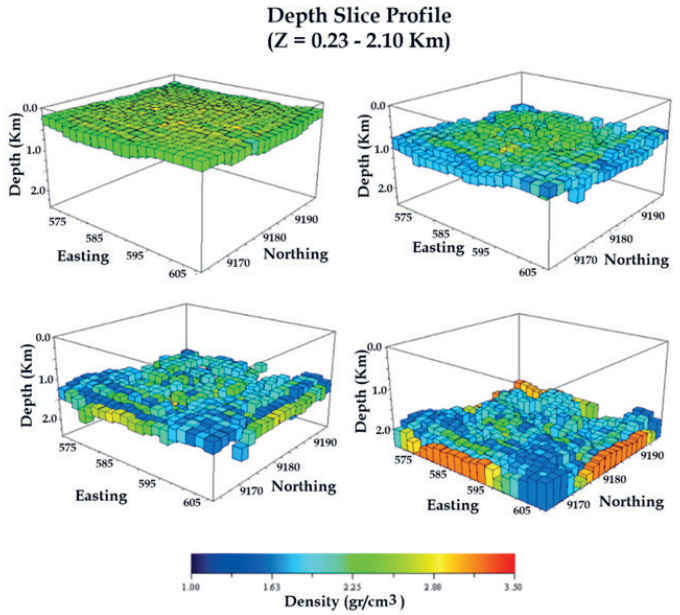

Figure 13. Cross-sectional incision profiles perpendicular to the Z-axis at 0.23, 0.91, 1.36 and 2.10 km depth, color-coded for density contrast (1.00–3.50 g/cm^3; blue to red).

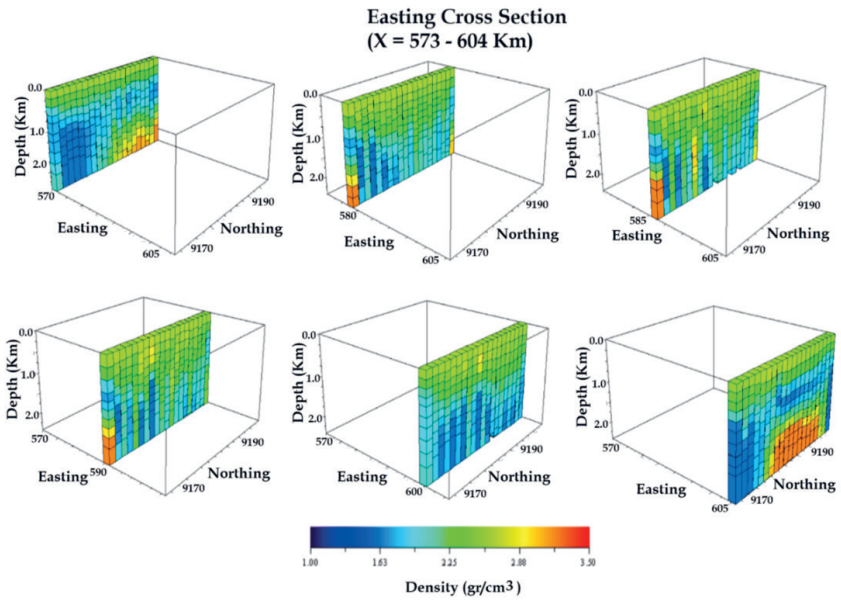

Figure 14. Cross-sectional incision profile perpendicular to the X-axis, illustrating the internal structure and layer arrangement.

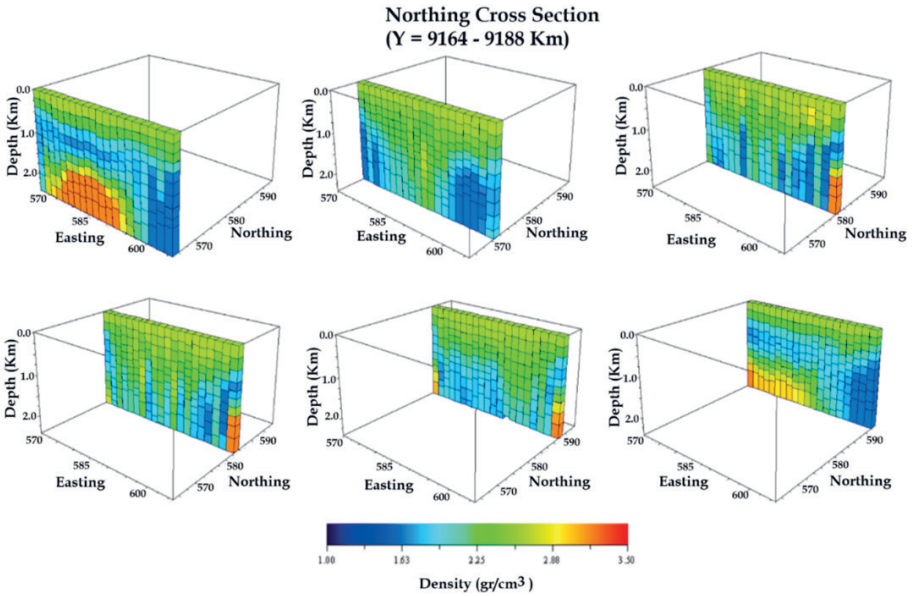

Figure 15. Cross-sectional incision profile perpendicular to the Y-axis, illustrating the internal structure and layer arrangement.

As noted by Telford (1990), geological maps, rock density data, and structural information are essential for interpreting subsurface features through 3D inversion modeling. Table 1 summarizes the key findings, including:

- Rock density values
- Block depth and vertical range
- Average density estimates

These parameters provide a quantitative basis for characterizing the subsurface geology and assessing geothermal potential.

Table 1. Average density of rocks at each depth.

n-Layer	Depth (km)	Density range (g/cm^3)	Average (g/cm^3)
1	0.00 – 0.23	2.551 – 2.689	2.617
2	0.23 – 0.46	1.986 – 2.670	2.368
3	0.46 – 0.69	1.391 – 2.534	1.929
4	0.69 – 0.91	1.563 – 2.090	1.592
5	0.91 – 1.14	1.314 – 2.238	1.764
6	1.14 – 1.36	1.574 – 2.734	2.493
7	1.36 – 1.59	1.453 – 2.709	2.639
8	1.59 – 1.82	1.435 – 3.500	3.029
9	1.82 – 2.10	1.459 – 3.500	3.128
10	2.10 – 2.43	1.457 – 3.456	3.498

In geothermal systems, caprock refers to an impermeable layer that overlies the reservoir, acting as a seal to prevent the upward migration of geothermal fluids. This barrier is critical for maintaining pressure and fluid retention within the geothermal reservoir.

In this study, the caprock is represented by layers 1 and 2, with average densities ranging from 1.9 to 2.68 g/cm^3 (depicted in green). These layers are interpreted to consist of limestone, dense sandstone, and impermeable claystone, forming a structural cover that supports the sustainability and isolation of subsurface thermal fluids.

The third, fourth, and fifth layers, with densities ranging from 1.31 to 2.23 g/cm^3 (shown in blue), are interpreted as the geothermal reservoir zone. These permeable layers likely contain soil, clay, sand, and conglomerate, which facilitate the storage and production of geothermal fluids for energy extraction.

The sixth and seventh layers, with densities between 2.4 and 2.8 g/cm^3, also function as caprock at greater depths. These layers are interpreted to contain marl, volcanic breccia, calcarenite, and granite. Upward-tapering rock intrusions observed within these layers suggest the presence of an active thrust fault in the Mount Pandan area, contributing to structural complexity and potential fluid migration pathways.

The eighth, ninth, and tenth layers represent the heat source zone, with densities reaching 3.5 g/cm^3. These layers are interpreted to contain basalt, peridotite, and magma, providing sufficient thermal energy within the crust to sustain geothermal activity.

4. Conclusion

Data processing and three-dimensional gravity inversion modeling reveal critical insights into the tectono-magmatic architecture of the Kendeng Zone. Low-density anomalies that align with hot-spring clusters underscore the role of Kendeng Fault activity in controlling magmatic ascent pathways. This interpretation is reinforced by shallow seismicity ($M < 4.0$) localized along strike-slip and oblique-reverse fault segments, which likely facilitate melt migration. The inversion delineates four discrete subsurface units: an upper caprock layer (0–0.46 km) with densities of 1.69–2.69 g/cm^3 attributable to pyroxene andesite; a reservoir horizon (0.46–1.14 km) characterized by 1.31–2.23 g/cm^3 densities consistent with sand–clay assemblages; a mid-crustal caprock–intrusion complex (1.14–1.59 km) exhibiting 2.4–2.8 g/cm^3 densities reflecting andesitic caprock intruded by volcanic breccia along active faults; and a deep-seated heat-source domain (1.59–2.43 km) with densities spanning 1.43–3.45 g/cm^3, indicative of basaltic intrusions and partial melt zones. Together, these findings illuminate how fault-controlled deformation dictates the spatial distribution of lithologies and magmatic bodies, thereby governing the geothermal potential of this convergent-margin system.

Authors' contributions

Eko Minarto: Conceptualization; methodology development; data curation; gravity data processing and inversion; FFD and derivative analyses; visualization; figures and tables preparation; writing — original draft, review & editing; project administration.

Krystallyn Gracella Angeline: Data acquisition and validation; DEM and lineament mapping; seismicity and focal-mechanism compilation; figures and tables preparation.

Both authors read and approved the final manuscript and agree to be accountable for all aspects of the work.

References

Agna, N. and Jati, W. W. (2021): Geology and geochemistry for medium enthalpy geothermal system of Mount Pandan, in: *Proceedings World Geothermal Congress 2020+1*, Reykjavik, Iceland, April – October 2021.

Alawiyah, S., Kadir, W. G. A., Santoso, D., Wahyudi, E. J., Aji, W. and Gunawan, I. (2022): Modeling of subsurface structure by using magnetic methods in the area of Mt. Pandan, Indonesia, *Arab. J. Geosci.*, **15**(15), 1330, https://doi.org/10.1007/s12517-022-10599-0.

d'Amour Uwiduhaye, J., Mizunaga, H. and Saibi, H. (2018): Geophysical investigation using gravity data in Kinigi geothermal field, northwest Rwanda, *J. Afr. Earth Sci.*, **139**, 184–192, https://doi.org/10.1016/j.jafrearsci.2017.12.016.

Dilalos, S., Alexopoulos, J. D. and Tsatsaris, A. (2018): Calculation of building correction for urban gravity surveys. A case study of Athens metropolis (Greece), *J. Appl. Geophys.*, **159**, 540–552, https://doi.org/10.1016/j.jappgeo.2018.09.036.

Frey, M., Bär, K., Stober, I., Reinecker, J., Van Der Vaart, J. and Sass, I. (2022): Assessment of deep geothermal research and development in the Upper Rhine Graben, *Geotherm. Energy*, **10**(1), 18, https://doi.org/10.1186/s40517-022-00226-2.

Guo, L., Meng, X., Chen, Z., Li, S. and Zheng, Y. (2013): Preferential filtering for gravity anomaly separation, *Comput. Geosci.,* **51**, 247–254, https://doi.org/10.1016/j.cageo.2012.09.012.

Harsolumakso, A. H., Noeradi, D., Rudyawan, A., Amiarsa, D., Wicaksono, S. and Nurfarhan, A. A. (2019): Geology of the Eastern Part of the volcanic-Kendeng zone of East Java: Stratigraphy, structures and sedimentation review from Besuki and Situbondo areas, *Jurnal Geologi dan Sumberdaya Mineral*, **20**(3), 143–152, https://doi.org/10.33332/jgsm.geologi.v20i3.465.

Heap, M. J. and Violay, M. E. S. (2021): The mechanical behaviour and failure modes of volcanic rocks: A review, *Bull. Volcanol.,* **83**(5), 33, https://doi.org/10.1007/s00445-021-01447-2.

Hutchings, S. J. and Mooney, W. D. (2021): The seismicity of Indonesia and tectonic implications, *Geochem. Geophys. Geosyst.*, **22**(9), e2021GC009812, https://doi.org/10.1029/2021GC009812.

Ibrahim, E., El-Motaal, A., Lashin, A., Alfaifi, H., Qaysi, S. and Kahal, A. (2021): Faulting E. intersections and magma-feeding zones in Tihamat-asir, Southeast red sea rift: Aeromagnetic and structural perspective, *J. Afr. Earth Sci.*, **173**, 104044, https://doi.org/10.1016/j.jafrearsci.2020.104044.

Jain, S. (2014): Earthquakes, in: *Fundamentals of Physical Geology*, *Springer Geology*. Springer India, New Delhi, 337–369, https://doi.org/10.1007/978-81-322-1539-4_15.

Khan, M. A. (2013): Seismology and earthquake effects for engineers, in: *Earthquake-Resistant Structures*, Elsevier, 29–56, https://doi.org/10.1016/B978-1-85617-501-2.00002-X.

Loshin, D. (2011): Data profiling, in: *The Practitioner's Guide to Data Quality Improvement*, Elsevier, 241–259, https://doi.org/10.1016/B978-0-12-373717-5.00014-2.

Minarto, E. and Azhari, N. Y. (2021): Application of moving average (MA) and upward continuation methods to Bouguer gravity anomaly data for fault analysis of the earthquake risk area of Timor and Flores Islands, *J. Phys.: Conf. Ser.*, **1951**(1), 012051, https://doi.org/10.1088/1742-6596/1951/1/012051.

Muttaqy, F., Nugraha, A. D., Mori, J., Puspito, N. T., Supendi, P. and Rohadi, S. (2022): Seismic imaging of lithospheric structure beneath central-east Java region, Indonesia: Relation to recent earthquakes, *Front. Earth Sci.*, **10**, 756806, https://doi.org/10.3389/feart.2022.756806.

Nakano, M., Citak, S. and Kalafat, D. (2015): Focal mechanism determinations of earthquakes along the North Anatolian fault, beneath the Sea of Marmara and the Aegean Sea, *Earth. Planet Sp.*, **67**(1), 159, https://doi.org/10.1186/s40623-015-0330-z.

Nowell, D. A. G. (1999): Gravity terrain corrections – An overview, *J. Appl. Geophys.*, **42**(2), 117–134, https://doi.org/10.1016/S0926-9851(99)00028-2.

Oberndorfer, H. and Müller, J. (2002): GOCE closed-loop simulation, *J. Geodyn.*, **33**(1–2), 53–63, https://doi.org/10.1016/S0264-3707(01)00054-0.

Oktoberiman, Ramadhan P, D. A., Rizki W, F. and Tawakal. A, R. (2015): Identification of geothermal potential based on Fault Fracture Density (FFD), geological mapping and geochemical analysis, case study: Bantarkawung, Brebes, Central Java, *KnE Energy*, **2**(2), 141–151, https://doi.org/10.18502/ken.v2i2.369.

Ramadhani, H., Wijayanti, H. D. K. and Trisnaning, P. T. (2018): Geokimia Daerah Panasbumi Gunung Pandan, Kabupaten Bojonegoro, Jawa Timur, *Jurnal Geosains dan Teknologi*, **1**(3), 107-112, https://doi.org/10.14710/jgt.1.3.2018.107-112 (in Indonesian).

Scandone, R., Cashman, K. V. and Malone, S. D. (2007): Magma supply, magma ascent and the style of volcanic eruptions, *Earth Planet. Sci. Lett.*, **253**(3–4), 513–529, https://doi.org/10.1016/j.epsl.2006.11.016.

Setyawan, A. (2022): Gravity inversion modelling using simulated annealing and the Levenberg-Marquardt algorithm, *International Journal of GEOMATE*, **23**(98), 109-116, https://doi.org/10.21660/2022.98.3518.

Stauder, S. J. W. (1962): The focal mechanism of earthquakes, in: *Advances in Geophysics*, **9**, Elsevier, 1–76, https://doi.org/10.1016/S0065-2687(08)60527-0.

Sumintadireja, P., Dahrin, D. and Grandis, H. (2018): A note on the use of the Second Vertical Derivative (SVD) of gravity data with reference to Indonesian cases, *J. Eng. Technol. Sci.*, **50**(1), 127–139, https://doi.org/10.5614/j.eng.technol.sci.2018.50.1.9.

Susilawati, A. Niode, M., Surmayadi, M., Pratomo, P. M., Nurhasan, Mustopa, E. J., Sutarno, D. and Srigutomo, W. (2023): Resistivity and density structure of Limboto Lake—Pentadio, Gorontalo, Indonesia based on magnetotelluric and gravity data, *Appl. Sci.*, **13**(1), 644, https://doi.org/10.3390/app13010644.

Takashima, I. and Yudiantoro, D. F. (2019): Magmatism and geothermal potential in Pandan Volcano East Java Indonesia, *Jurnal Mineral, Energi dan Lingkungan*, **2**(2), 50-60, https://doi.org/10.31315/jmel.v2i2.2214.

Tang, H. and Sun, W. (2021): A discussion of the Bouguer correction, *Pure Appl. Geophys.*, **178**(9), 3543–3557, https://doi.org/10.1007/s00024-021-02816-w.

Thoha, M., Parman, P., Prastistho, B., Yudiantoro, D. F., Hati, I. P. and Jagranata, I. B. (2014): Geology and geothermal manifestations of Mount Pandan, East Java, in: *Proceedings of 3rd International ITB Geothermal Workshop* 2014 Institut Teknologi Bandung, Bandung, Indonesia, March 3–7, pp 13, available at http://eprints.upnyk.ac.id/14608/1/4.%20Maret%202014%20CD%20GEOLOGY%20AND%20GEOTHERMAL%20MANIFESTATIONS%20OF%20MOUNT%20PANDAN%2C%20EAST%20JAVA.pdf.

Wang, N., Chang, H. and Zhang, D. (2023): Inverse modeling for subsurface flow based on deep learning surrogates and active learning strategies, *Water Resour. Res.*, **59**(7), e2022WR033644, https://doi.org/10.1029/2022WR033644.

SAŽETAK

Kvantificiranje podzemnih rasjeda pomoću mjerenja seizmičke aktivnosti i gravitacijskog polja na planini Pandan, Indonezija

Eko Minarto i Krystallyn Gracella Angeline

Indonezija, koja se prostire između 6° sjeverne i 11° južne geografske širine te 95° i 141° istočne geografske dužine, je podložna intenzivnoj vulkanskoj i tektonskoj aktivnosti zbog susretanja nekoliko velikih tektonskih ploča. Fiziografski, planina Pandan smještena je u području modernog Sundskog luka unutar Antiklinorija ili Kendeng zone. Prethodna istraživanja zabilježila su manji potres 2016. godine u Kendeng zoni, što ukazuje na kontinuiranu tektonsku aktivnost povezanu s podmagmatskom aktivnošću opaženom u nekoliko termalnih izvora u područjima Banyukuning, Jari i Selogajah. Koristeći podatke gravitacije, utvrđujena je povezanost između tektonske i magmatske aktivnosti putem 3D inverzijskog modeliranja podzemnih struktura. Ova analiza povezuje se s gustoćom rasjednih pukotina na površinama s rasjedima ili pukotinama, pri čemu je identifikacija žarišnog mehanizma ključna za definiranje modela rasjeda izvorišta potresa. Gibanje Zemljine kore duž Kendeng rasjeda utječe na podložne magmatske procese, a dokazi za to se uočavaju kroz zone niske gustoće i putem podmagmatskih značajki, poput prisutnosti termalnih izvora. Potresi oko planine s magnitudama manjim od 4,0 SR upućuju na povezanost gibanja strike-slip rasjeda i kosih reversnih rasjeda s uzdizanjem magme.

3D inverzijsko modeliranje otkriva četiri sloja:

- Na dubini od 0–0,46 km, s procijenjenim rasponom gustoće 1,69–2,69 g/cm^3, sloj tumačimo kao krovnu stijenu, sastavljenu od piroksena i okolnih stijena.
- Sloj na 0,46–1,14 km, s gustoćom 1,31–2,23 g/cm^3, tumači se kao rezervoar koji sadrži pijesak i glinovite stijene.
- Andesitne i vulkanske breče čine sloj na 1,14–1,59 km, s gustoćom 2,4–2,8 g/cm^3. Smatra se da se radi o krovnoj stijeni i intruziji (aktivni rasjed).
- Sloj na 1,59–2,43 km, s gustoćom 1,43–3,45 g/cm^3, tumačimo kao izvor topline s bazaltnim stijenama i magmatskim sadržajem.

Ovi nalazi pružaju nove uvide u podzemnu strukturu i dinamiku rasjeda u Kendeng zoni, doprinoseći boljem razumijevanju tektono-magmatskih interakcija u seizmički aktivnim regijama.

Ključne riječi: Kendengski rasjed, planina Pandan, podaci o gravitaciji, spremište, potres

Corresponding author's address: Eko Minarto, Department of Physics, Sepuluh Nopember Institute of Technology, Surabaya, 60111, Indonesia; e-mail: minarto@physics.its.ac.id